physica status solidi b
www.pss-b.com

Ni-Alloyed Copper Iodide Thin Films: Microstructural Features and Functional Performance

Christiane Dethloff, Katrin Thieme, Susanne Selle, Michael Seifert, Sofie Vogt, Daniel Splith, Silvana Botti, Marius Grundmann,* and Michael Lorenz**

To tailor electrical properties of often degenerate pristine CuI, Ni is introduced as alloy constituent. Cosputtering in a reactive, but also in an inert atmosphere as well as pulsed laser deposition (PLD), is used to grow $Ni_xCu_{1-x}I$ thin films. The Ni content within the alloy thin films is systematically varied for different growth techniques and growth conditions. A solubility limit is evidenced by an additional $NiI_2(H_2O)_6$ phase for Ni contents $x \geq 0.31$, observed in X-Ray diffraction and atomic force microscopy by a change in surface morphology. Furthermore, metallic, nanoscaled nickel clusters, revealed by X-Ray photoelectron spectroscopy and high-resolution transmission electron microscopy (HRTEM), underpin a solubility limit of Ni in CuI. Although no reduction of charge carrier density is observed with increasing Ni content, a dilute magnetic behavior of the thin films is observed in vibrating sample magnetometry. Further, independent of the deposition technique, unique multilayer features are observed in HRTEM measurements for thin films of a cation composition of $x \approx 0.06$. Opposite to previous claims, no transition to n-type behavior was observed, which was also confirmed by density functional theory calculations of the alloy system.

1. Introduction

CuI is a promising candidate for complementary devices, when combined with n-type semiconductors, such as GaN or ITO, as it offers outstanding intrinsic opto-electrical properties among the *p*-type semiconducting materials. Its potential is characterized by transparency in the visible spectrum, a bandgap of 2.95 eV at room temperature (RT), and a high hole mobility of $\mu = 44\,cm^2V^{-1}s^{-1}$ as reported for single crystals,[1] exceeding that of other *p*-type materials.[2,3] Hole concentrations as high as $p = 10^{20}cm^{-3}$ have been achieved in thin films.[4,5]

However, to date CuI, thin films are not yet applied as active layer in thin-film electronics, like diodes or transistors. The reason for that is the high charge carrier density and its low resistivity, which prevent the formation of a depletion region within the CuI. This degenerate charge carrier density is often attributed to copper vacancies (V_{Cu}),[5,6] but recently also to oxygen diffusion from the environment.[7,8] Doping or alloying binary CuI with Zn, Ag, Ni, Sn or Se has already been shown to cause electronic defect states, which enable adjustments of the morphological, optical, and electrical properties.[9–13]

Of special interest are recently published results about the $Ni_xCu_{1-x}I$ alloy. A steady decrease of the charge density for a Ni fraction $0 \leq x \leq 0.10$ is observed.[10] For Ni fractions $0.15 \leq x \leq 0.35$, there even seems to be a transformation into an n-type semiconductor. This could predestine $Ni_xCu_{1-x}I$ for homojunction devices, consisting of a binary CuI *p*-type layer and an n-type ternary $Ni_xCu_{1-x}I$ layer, if the results from ref. [10] can be reproduced.

Furthermore, a transition from diamagnetic pristine CuI to a dilute magnetic $Ni_xCu_{1-x}I$ alloy was shown in ref. [10]. Research concerning dilute magnetic semiconductors (DMS) is a quickly growing and comprehensive field within material research, due to remarkable properties for applications in quantum technology, like spin injection or control of the magnetic field by induced electrical currents or fields.[14] As most of the recently known DMS consist of (II–VI) or (III–V) host lattices[14] with incorporated transition metals, the (I–VII) configuration of CuI would be a novelty in the field.

Aim and motivation of this work is trying to reproduce the promising results of Annadi et al.[10] and in particular to gain

C. Dethloff, S. Vogt, D. Splith, M. Grundmann, M. Lorenz
Felix-Bloch-Institut für Festkörperphysik
Universität Leipzig
Linnéstr. 5, 04103 Leipzig, Germany
E-mail: christiane.dethloff@physik.uni-leipzig.de;
grundmann@physik.uni-leipzig.de; mlorenz@physik.uni-leipzig.de

K. Thieme, S. Selle
Optical Materials and Technology
Fraunhofer Institute for Microstructure of Materials and Systems IMWS
Walter-Huelse-Strasse 1, Halle (Saale) 06120, Germany

M. Seifert, S. Botti
Institut für Festkörpertheorie und –optik
Friedrich-Schiller-Universität Jena
Max-Wien-Platz 1, 07743 Jena, Germany

S. Botti
Research Center Future Energy Materials and Systems of the Research Alliance Ruhr
Faculty of Physics and ICAMS
Ruhr University Bochum
Universitätsstraße 150, 44780 Bochum, Germany

DOI: 10.1002/pssb.202300492

more insights on the claimed transition from *p*- to n-type conductivity within the $Ni_xCu_{1-x}I$ alloy. Therefore, we performed a comprehensive growth study of $Ni_xCu_{1-x}I$ thin films, engaging two different deposition techniques: reactive magnetron cosputtering and pulsed laser deposition (PLD). By doing that, we are able to distinguish inherent microstructural properties of the alloy system and growth technique-related alloy properties. Having these capacities is very powerful, when studying a novel material, such as $Ni_xCu_{1-x}I$, which has been rarely reported before.[10]

All thin films are characterized structurally, optically, and electrically to gain a profound understanding of the $Ni_xCu_{1-x}I$ alloy. The main focus in this article is on the results of reactively cosputtered thin films, which are underpinned by results of the PLD thin films in the Supporting information.

2. Results

2.1. Structural Properties

By reactive cosputtering, $Ni_xCu_{1-x}I$ thin films with varying Ni fractions have been fabricated. For all thin films, the structural properties were investigated by X-ray diffraction (XRD) measurements, as is shown in **Figure 1a** for an extracted range of 15°–40° obtained by 2θ–ω scans. It can be seen that the reflex of the (111)-plane of γ-CuI is prevalent for every thin film, without exhibiting a systematic shift in peak position as a function of Ni fraction (Figure 1b), inconsistent with literature.[10] This contradicts a homogeneous incorporation of Ni into CuI, as a shift in lattice spacing, and thus peak position is expected through radii and valency effects. In accordance with the results of sputtered $Ni_xCu_{1-x}I$ thin films, no shift of the γ-CuI (111)-plane reflex has been observed for the PLD thin films (Figure S1, Supporting Information).

An additional reflex and its repetition is observed in the X-Ray diffractogramms (Figure 1a) at 2θ=18.2° and 2θ=36.8°, which can be attributed to the nickel iodide hydrate ($NiI_2(H_2O)_6$) (001)-plane. As this additional phase only occurs for thin films of Ni contents $x \geq 0.31$, a solubility limit for the Ni within the CuI host lattice can be concluded. Excess Ni may accumulate together with iodine on top of the $Ni_xCu_{1-x}I$ thin film to form deliquescent NiI_2 and eventuate in $NiI_2(H_2O)_6$ when exposed to humidity of the ambient atmosphere. This is further supported by the visual appearance of the thin films after deposition, which is shown in Figure S2, Supporting Information. Directly after growth, thin films with high nickel content exhibit a black color, which turns transparent upon contact with ambient atmosphere and thus humidity. This was also reported by Siegler et al.[15] as a characteristic of NiI_2 thin films. The discoloration is reversed by desorption of H_2O, when the thin films are stored in N_2 atmosphere of an desiccator, also in accordance with ref. [15].

The topography of the thin films was studied by atomic force microscopy (AFM) measurements, which are depicted in **Figure 2**. For Ni contents of $x \leq 0.05$, the typical triangular-shaped crystallites of γ-CuI are detected (Figure 2a), which become more rounded for $x = 0.12$ (Figure 2b). In accordance with the XRD results (Figure 1a), a second phase is detected for $x = 0.31$ (Figure 2c), which dominates on the surface for $x \geq 0.34$ (Figure 2d). This is a further indication that the $NiI_2(H_2O)_6$ phase forms at the surface of the thin films. Furthermore, a decreased crystallite size of the γ-CuI crystallites is recognized for the thin film with an elevated Ni content of $x = 0.31$, which is also described for reference thin films in literature.[10] The surfaces of the depicted thin films in Figure 2 exhibit a root mean square roughness in the range $R_q = 15.4 \ldots 24.3$ nm, as labeled.

2.2. Valence State

Analyses regarding the valence state of Ni within reactively cosputtered $Ni_xCu_{1-x}I$ thin films were performed via X-Ray photoelectron spectroscopy (XPS). If the valence state of Ni is elevated, compared to Cu^+ in binary CuI, the hole concentration can be reduced by incorporation of Ni, as claimed in ref. [10]. Thus, determining the chemical state is indispensable in this study. Additionally, further information on the secondary $NiI_2(H_2O)_6$ phase can be gained. Therefore, four reactively cosputtered $Ni_xCu_{1-x}I$ thin films of different Ni concentrations $x = 0.01$, 0.06, 0.26, and 0.71 were investigated by XPS on the surface as well as in the bulk.

Because of multiplet splitting, shake up, and plasmon loss structures being prevalent in many transition metal oxides,[16] the valence state of Ni cannot be derived solely by the analysis of the element-specific binding energies E_B. Additionally, there

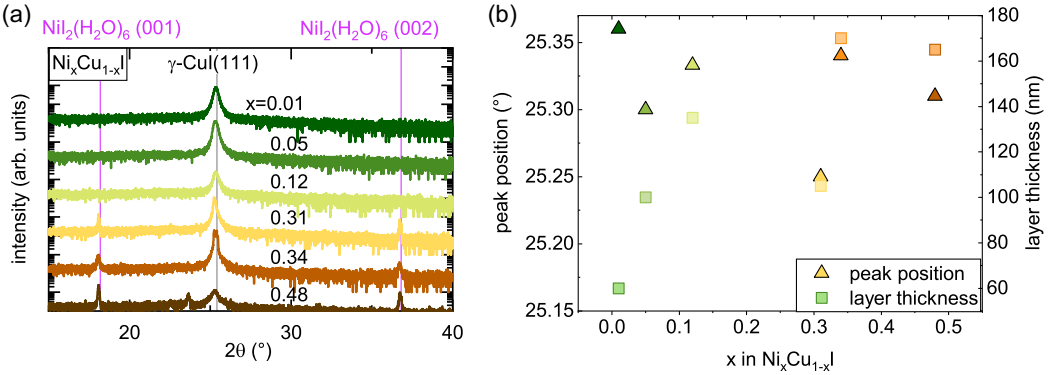

Figure 1. a) X-Ray diffractograms of reactively cosputtered $Ni_xCu_{1-x}I$ thin films on glass substrates with varying Ni contents *x* as denoted in an extracted range from 15 to 40°. b) Position of the (111)-plane peak of the prevalent γ-CuI and thin-film layer thickness, both depending on the Ni fraction, detected via EDX spectroscopy.

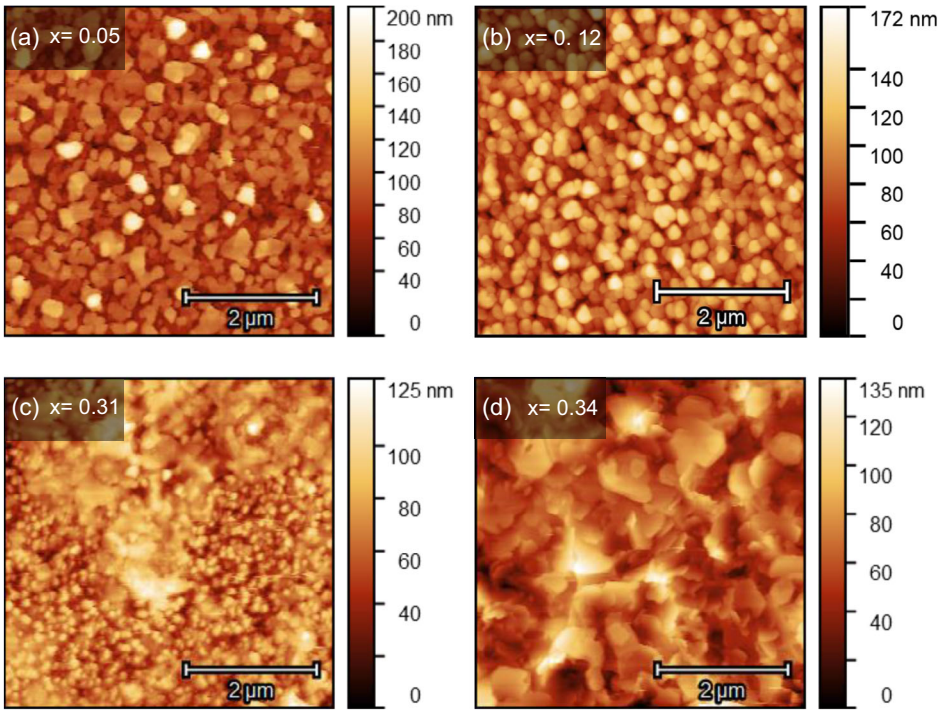

Figure 2. Surface images of reactively cosputtered $Ni_xCu_{1-x}I$ on glass substrates obtained via AFM scans with varying Ni contents as denoted. R_q values are: a) 24.3nm, b) 23.7nm, c) 15.4 nm, and d) 19.4nm.

is an overlap of Ni $2p_{1/2}$ and I $3p_{1/2}$ (see Figure S3, Supporting Information), impeding a distinction between the two signals.

To enable the determination of the Ni valence state within the thin films, an additional Auger peak analysis has to be conducted, to obtain kinetic energy E_{kin}[17]. The determination of a modified Auger parameter proved as a valuable tool for investigations on the chemical state for Ni in metals, oxides, and halides; it also excludes charge effects, as specific advantage.[17] Consequently, the recorded data was visualized in 2D chemical state diagrams, also known as Wagner plots (**Figure 3**), where the kinetic energy E_{kin} of the sharpest Auger line (Ni LMM) is plotted against the binding energy E_B of the most intense photoelectron line (Ni $2p_{3/2}$).[18] The specific modified Auger parameter α' was calculated using $\alpha' = E_B + E_{kin}$.[17]

As shown in Figure 3a,b, the distribution of the measurement results within a Wagner plot is very narrow for all measured thin films. All of these points are in the vicinity of prototypical γ-NiOOH (Ni^{3+}) in Figure 3a and NiI_2 (Ni^{2+}) in Figure 3b, respectively. The comparability to NiI_2 matches the assumption of the $NiI_2(H_2O)_6$ phase being present on the surface of the thin films; the Ni is incorporated as Ni^{2+} in that case. There is no consistent explanation of the comparability to γ-NiOOH with the chemical state Ni^{3+} so far, except for possible, structural inhomogenities of the $NiI_2(H_2O)_6$.

In Figure 3c,d, the results of measurements in the bulk of the thin films are shown. As shown, the distribution is more spread and different results can be found for Ni-poor thin films ($x \leq 0.06$) and Ni-rich thin films ($x \geq 0.26$). The valence state of Ni in Ni poor thin films is comparable to NiO or NiI_2, respectively; in both cases the chemical state is Ni^{2+}, which accordingly should reduce the charge carrier density compared to binary CuI. This is in consistence with the results in literature.[10] However, Ni-rich thin films refer more to metallic Ni^0; thus, the solubility limit is expressed not only by a phase separation into $NiI_2(H_2O)_6$, but also metallic Ni clusters, which superimpose other signals in XPS measurements. For that reason, the valence state of Ni in a potentially coexisting $Ni_xCu_{1-x}I$ phase cannot be distinguished by XPS for Ni-rich thin films.

2.3. High-Resolution Transmission Electron Microscopy

As AFM, XRD, and XPS data showed clear differences depending on the Ni content, cross-sectional transmission electron microscopy (TEM) samples were prepared for thin films with a Ni content of $x = 0.02$, $x = 0.06$, and $x = 0.26$. These thin films were chosen in order to match with similar Ni contents in PLD-grown $Cu_xNi_{1-x}I$ films (Figure S4, and S5, Supporting Information). **Figure 4** shows overview TEM images of the samples by depicting the whole sample setup (labeled in Figure 4a).

The thin films with lower Ni concentration $x \leq 0.06$ show a similar morphology with grain size of about 500 nm and height varying between $\approx$ 350 nm (valley) and $\approx$ 600 nm (peak). The thin film with the elevated Ni content $x = 0.26$ however appears different, exhibiting a very porous structure, but smoother surface (smaller height variation between 600 and 700 nm). Instead of rather large, distinguishable grains, the film consists mainly of platelet-like flakes (height $10 - 20$ nm), which are layered on top of each other. Additionally, some large single-crystalline particles can be seen within the film (Figure 4f). It has to be considered that the large pores might be voids, left by those particles during

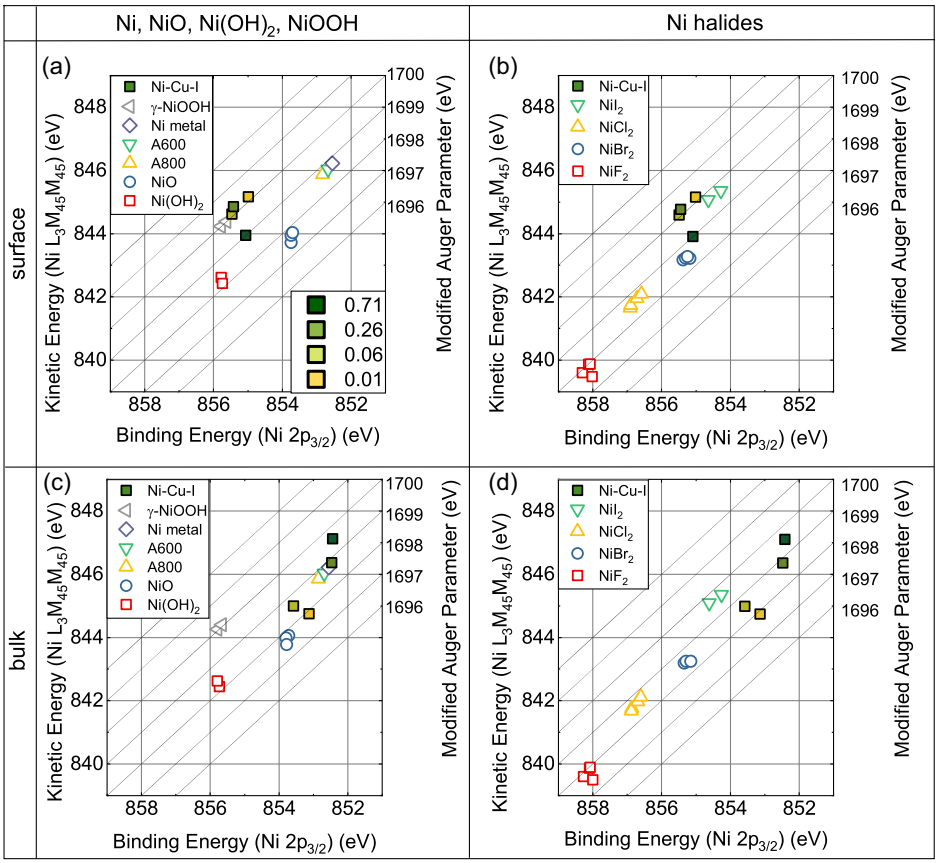

Figure 3. Wagner plots of acquired binding energies of Ni $2p_{3/2}$ and kinetic energies of Ni LMM within the $Ni_xCu_{1-x}I$ thin films with varying *x*-, as denoted. Results of analysis a,b) at the surface and c,d) in the bulk of the thin films as well as in comparison to a,c) NiO/NiOH references and b, d) Ni halides. A600 and A800 describe metallic Ni alloys, mostly consisting of Ni–Cr (A600) and Ni–Cr–Fe (A800) and are, like all other references, adapted from Biesinger et al.[17].

the focused ion beam (FIB) thinning process, when extracting the lamella from the original thin film. It is very likely that the XRD analysis of thin films with elevated Ni contents mainly gives information about these single-crystalline particles, as the small flakes with their differing orientations would not give rise to sharp peaks.

In some grains of the thin films with $x = 0.02$ and $x = 0.06$, as well as in the PLD-grown film with the lowest Ni content (Figure S4 and S5, Supporting Information), a layered structure with rather irregular intervals was detected ($10 - 30$ nm interval thickness, see Figure 4b,d)). High-annular dark-field (HAADF) scanning transmission electron microscopy (STEM) images of the reactively cosputtered thin films depict the described morphology even more clearly (Figure S6, Supporting Information). This feature indicates a cation segregation, which is not further investigated within the scope of this work, but needs to be studied systematically.

To compare the lattice parameters of the thin films with $x = 0.02$ and $x = 0.26$, electron diffraction patterns (EDPs) with a selected-area diffraction (SAD) aperture (10 mm size with a projected size of 200 nm) were taken and analyzed. For the thin film with $x = 0.02$, a homogeneous, that is, single-crystalline grain was chosen as the diffraction area, whereas for the thin film with $x = 0.26$, the SAD aperture was confined to an area within one of the single-crystalline particles (EDPs and tables see Figure S7, Supporting Information). Quantification of the reflexes, distances, and angles assigns both patterns to the γ-CuI phase.[19] As STEM-EDXS analysis will show later that nearly no Ni ($x \approx 0.01$) could be detected within these particles of the thin film with $x = 0.26$. This substantiates the XRD results that showed no correlation of lattice parameters and Ni content.

To obtain information about the homogeneity of the spatial distribution of the Ni, STEM–EDXS was carried out. **Figure 5** shows the HAADF images and elemental maps for each thin film. For the lowest Ni concentration within the thin films (Figure 5a), the Ni distribution is rather homogeneous. However, the correlation of Ni-rich layers with the layer structure detected with TEM and STEM can be clearly seen for Ni concentration of $x = 0.06$. Elemental maps of the thin film with $x = 0.26$ (Figure 5c) revealed another feature, which is not detected in TEM analysis: the nickel segregates into small clusters ($15 - 25$ nm size) throughout the thin film. Therefore, another high-resolution transmission electron microscopy (HRTEM) analysis was carried out at the areas of the Ni-rich clusters. Even though the TEM sample is most likely too thick and a projected overlay of differently orientated flakes could not be

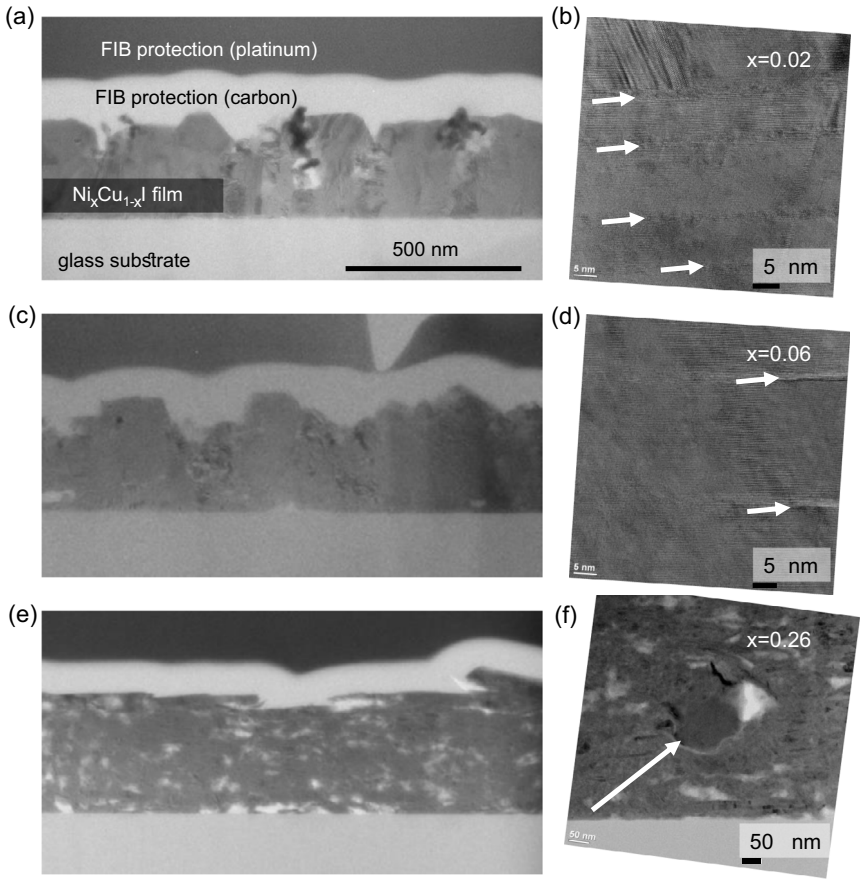

Figure 4. TEM overview images of reactively cosputtered thin films on glass substrates with Ni contents of a,b) $x = 0.02$, c,d) $x = 0.06$, and e,f) $x = 0.26$. The corresponding HRTEM images on the right side (b + d) show a specific feature: a layer structure in thin films with $x \leq 0.06$ (white arrows). For the thin film with $x = 0.26$ a larger TEM magnification is shown f), depicting the porous flake-like structure and one of the single-crystalline particles (white arrow).

avoided, it was possible for at least at one position to match the position of a Ni-rich cluster with an HRTEM image. By analyzing part of the atomic ordering, the cluster can be correlated to metallic Ni.[20] **Figure 6** shows the correlation between the composition map for Ni and HRTEM image together with an enlarged model of the appropriately oriented Ni phase (blue stick-and-ball model). This is in good agreement with the XPS results, which also yielded a signal for metallic Ni for $x \geq 0.26$.

Quantifying the global composition of the whole film area, including Ni-rich and Ni-poor parts by STEM–EDXS, yields comparable results to the data collected by top-view scanning electron microscopy–energy-dispersive spectroscopy (EDX) (SEM-EDX). This is expected, as the area from which the SEM-EDX signal is obtained is much larger to that in STEM-EDXs and thus yields an average value. Spatially resolved TEM and STEM–EDXS results could show that these global values do not represent the composition of a homogeneous film, but are integrated values of the compositions of locally distributed Ni-rich and Ni-poor parts within in the thin film. STEM–EDXS evaluation of the individual phases, that is, CuI particles and areas containing Ni-rich nanoclusters, revealed Ni shares far below the global Ni share, due to a lack of Ni within the CuI particles and well above it within the Ni nanoclusters, where $x \approx 0.5$. These results further emphasize the small solubility limit of Ni in CuI, at which a homogeneous thin film may still be obtained. Furthermore, in this work, the cation composition of each thin film was evaluated by analyses of the Ni and Cu K-lines, whereas in literature,[10] evaluation at the Ni and Cu L-Lines was performed. For further explanation, see Figure S8 to S10, Supporting Information.

2.4. Magnetic and Electrical Properties

2.4.1. Magnetic Properties

As Ni is a ferromagnetic element, the magnetic properties of $Ni_xCu_{1-x}I$ thin films have been investigated. Preliminary estimations about the resulting saturation of the magnetic moment, consider the exchange of Cu cations within the zincblende γ-CuI unit cell (u.c.). For a homogeneously grown $Ni_{0.25}Cu_{0.75}I$ thin film, one Cu atom is replaced by Ni, which would result in $M_{sat} = 0.6\,\mu_B/u.c.$ at $T = 0\,K$. In a $Ni_{0.5}Cu_{0.5}I$ alloy, the exchange of two atoms per u.c. is considered and the theoretical maximum saturation moment yields $M_{sat} = 1.21\,\mu_B/u.c.$ at $T = 0\,K$. Three thin films with $x = 0.12$, $x = 0.31$, and $x = 0.48$ were further characterized by vibrating sample magnetometry (VSM).

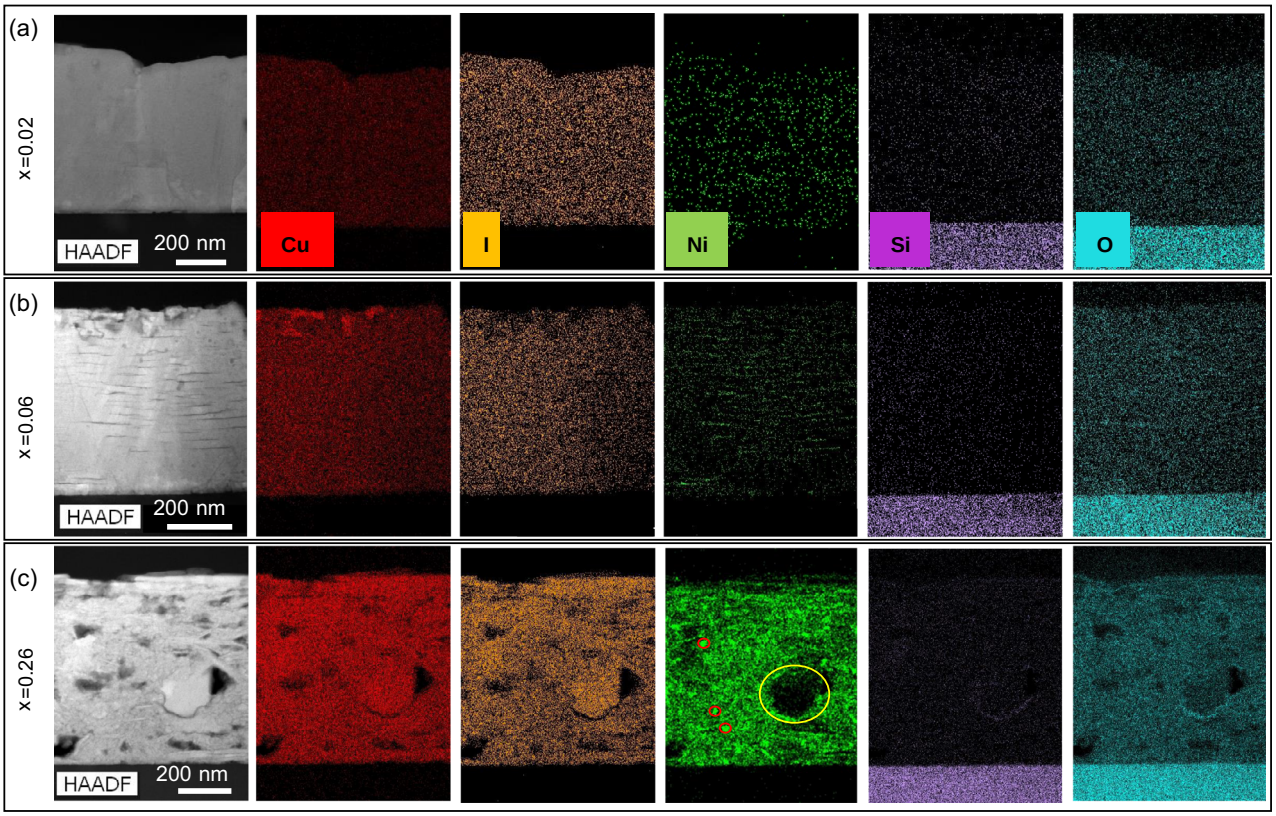

Figure 5. a) Elemental maps of reactively cosputtered thin films on glass substrates for varying Ni contents (as labeled) for Cu–K, I–L, Ni–K, Si–K, and O–K. In b), there is a more distinct layer structure with Ni-rich and Ni-deficient layers, whereas in c), there are even two additional types of features: CuI particles (encircled yellow) and nanoscaled Ni-rich clusters (encircled red).

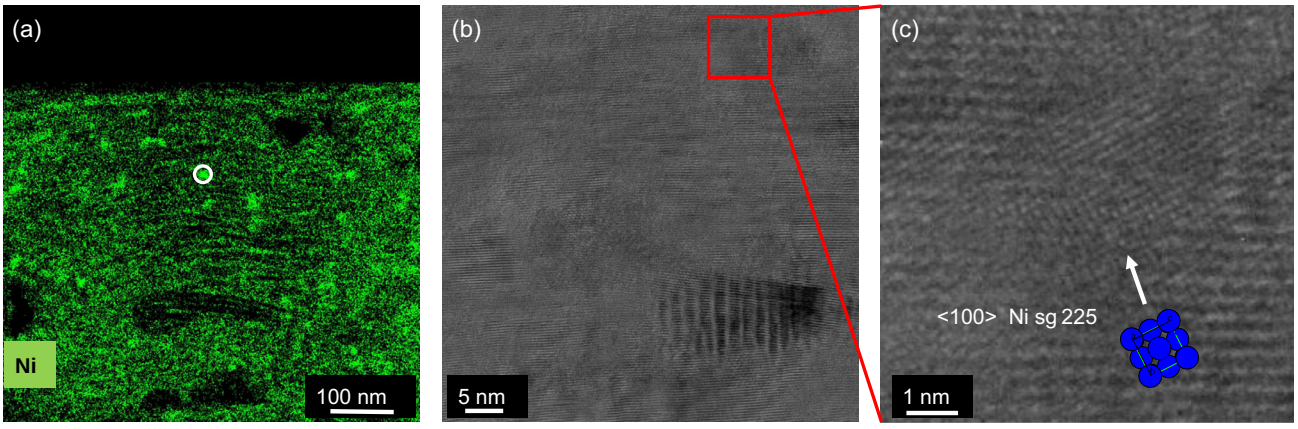

Figure 6. a) Ni map (counts - deconvoluted and averaged) of the same thin film as in Figure 5c shows small Ni-rich clusters (white encircled), b) HRTEM image of Ni-enriched area, and c) Enlarged part of (b) showing atomic ordering (white arrow) with enlarged model of the appropriately oriented Ni phase.

For all measured thin films, a saturation of the magnetic moment at $T = 50$ K is observed, which indicates a ferromagnetic behavior within each thin film (see **Figure 7**). The magnitude of the $Ni_{0.48}Cu_{0.52}I$ thin film is about $M = 0.27\,\mu_B/u.c$ and therefore about 4.5 times smaller than the gauged value. However, it is about an order of magnitude larger compared to the thin films with $x \leq 0.31$, where a dilute magnetic behavior is observed. This difference in magnitude can be explained by the presence of nanoscaled Ni clusters within the $Ni_{0.48}Cu_{0.52}I$ thin film, which additionally contributes to the magnetic moment besides the dilute magnetic behavior of the $Ni_xCu_{1-x}I$ alloy. This is underpinned by XPS and HRTEM measurements, which revealed the presence of metallic Ni in thin films with an elevated Ni content.

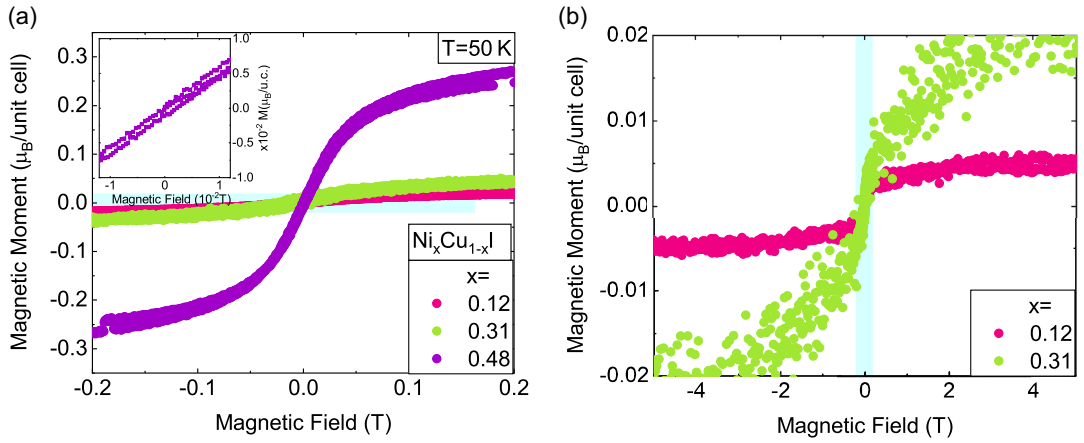

Figure 7. a) Magnetization curves of $Ni_xCu_{1-x}I$ thin films deposited by reactive cosputtering on glass substrates with varying Ni content x as denoted. b) Magnetization curves in the extended range of the external magnetic field, where a paramagnetic contribution of the depicted films can be seen in the high-field regime. The blue stripe refers to the range, which is depicted with a higher resolution in the respective other diagram for better understanding.

As shown in the inset diagram of Figure 7a, no hysteresis is measured, which is unlikely for ferromagnetism, but also reported for other DMS materials.[21,22] However, the absent hysteresis can also be explained by the spatial distribution of the nanoscaled Ni clusters, where their Weiss domains may be isolated and not able to interact with each other.

Regarding the $NiI_2(H_2O)_6$ phase, its anhydrous state NiI_2 is reported antiferromagnetic below a Néel temperature of $T_N = 75$ K at $p = 0$ mbar,[23] so no contribution to the magnetization curve is expected. For increased measurement temperatures (not shown), a paramagnetic contribution is expected, but not evaluated, as each linear contribution is removed in the data processing. Although measurements have been conducted in a temperature range from 50 to 300 K, no dependence onto the magnetization curve was observed. Therefore, the results of higher temperatures are not shown here.

Compared to thin films of equal Ni contents in literature,[10] the thin films of this work exhibit a magnetization moment, which is about four times higher at the saturation field strength of the thin film $Ni_{0.48}Cu_{0.52}I$ of $H = \pm 0.2$ T. An explanation for the suppressed magnetic moment in literature could be that the thin-film compositions have been detected by EDX at an excitation energy of $E = 10$ keV[10], where the signals of Ni–L and Cu–L overlap and therefore the Ni content is overestimated (Figure S8–S10, Supporting Information).

2.4.2. Electrical Properties

All thin films were characterized electrically to systematically determine an influence of the Ni incorporation on the electrical properties of CuI. To gain a more profound understanding of the alloy, results obtained for different deposition techniques within this work as well as literature values[10] are depicted in **Figure 8**a. Figures 8b–d shows resistivity, Hall mobility, and hole densities, extracted from Hall effect and conductivity measurements. The different growth series and deposition techniques are color coded and marked by shape, as denoted.

First, for each of the growth series, a trend of increasing resistivity with increasing Ni content is observed (Figure 8a). However, not only the Ni content determines the resistivity, but the biggest influence is exerted by the deposition conditions. Comparing the resistivity of thin films with $x \approx 0.05$, a range of two orders of magnitude is covered, from $\rho = 0.02\,\Omega$ cm (DC/DC sputtering mode) to $\rho = 2.70\,\Omega$ cm (elevated temperature of $T = 130\,^{\circ}C$).

Second, as shown in Figure 8b–d, only measured thin films of a reduced Ni concentration $0 < x < 0.12$ result in reliable data, due to the resolution limit of the setup, and accordingly a degeneracy of all other thin films. Therefore, we assume that for higher concentrations $x > 0.12$, phase separation leads to a domination of the charge transport either by degenerate CuI or also probably by metallic Ni.

Third, the plotted values in the range $0 < x < 0.12$ reveal an increase in hole density and a decrease in resistivity as a function of Ni concentration. But, if Ni was incorporated into the CuI lattice and contributing to charge transport as donor (Ni^{2+}), a reduced charge carrier density and increased resistivity is expected, assuming no significant changes in charge carrier mobility. So the results contradict the preliminary considerations and observations from literature.[10]

Furthermore, no evidence for a transition into an n-type semiconducting behavior was observed, neither in Hall nor Seebeck effect measurements, within the whole growth study, which is again in contrast to literature.[10] Also a decrease in Hall mobility is denoted, which is unfavorable regarding a procession toward CuI–$Ni_xCu_{1-x}I$ p–n homojunctions. Due to these obtained results regarding the electrical properties of the $Ni_xCu_{1-x}I$ alloys with varying Ni content, no in situ p–n homojunctions were fabricated within this work.

The insights gained into the electrical properties of the $Ni_xCu_{1-x}I$ alloy are consistent with the findings from TEM, STEM–EDX, and XPS measurements. After an increase in hole density for lower Ni concentrations $0 < x < 0.12$, phase separation, especially into binary CuI and possibly also metallic Ni clusters, leads to a degeneracy of the $Ni_xCu_{1-x}I$ thin films. These results contradict the findings of Annadi et al.[10] as they claimed a decrease in hole density and a transition to n-type with

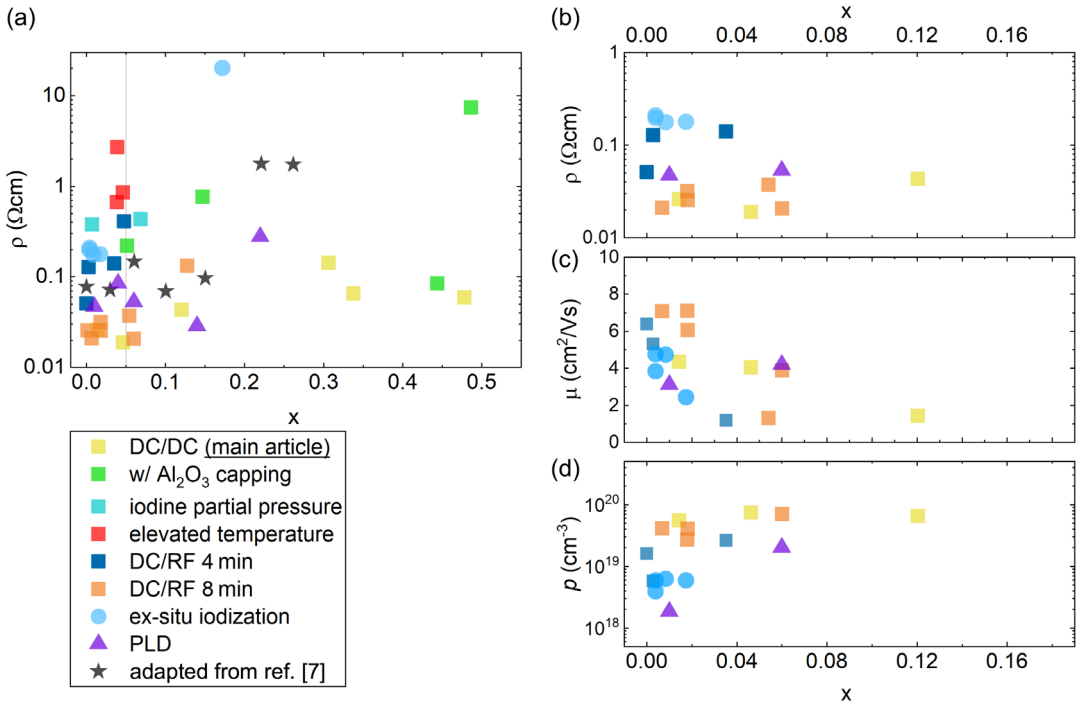

Figure 8. a) Resistivity ρ as a function of Ni fraction x in every deposited $Ni_xCu_{1-x}I$ fabricated within this work. The dependence on the varied process parameter is given by color code and different deposition techniques by varying shapes (square: reactive sputtering; circle: metallic sputtering and ex situ iodization; triangle: PLD; star, Adapted from ref. [10] (metallic cosputtering and ex situ iodization)), b) resistivity, c) Hall mobility, and d) hole concentration extracted from Hall effect and conductivity measurements within the resolution limit of the measurement setup.

increasing Ni content within the $Ni_xCu_{1-x}I$ alloy. A possible explanation is that the thin films in ref. [10] are also characterized by metallic Ni clusters, and the allegedly n-type behavior is a result of metallic Ni dominating the charge transport. A more differentiated statement is not possible, because the authors in ref. [10] didn't perform microstructural analyses, like TEM or STEM–EDX and their XPS analysis was insufficient regarding an evaluation of a transition metal alloy system. To substantiate our findings that the $Ni_xCu_{1-x}I$ alloy remains a *p*-type semiconductor, we employed density functional theory (DFT) calculations.

3. Computational Results

In reference to the potential shift toward n-type conductivity, the density of states (DOS) was computed using DFT and HSE06 functional with a modified mixing parameter (referred to as mHSE06; detailed methodology provided in the Computational Methods). This analysis was focused on ordered alloys with a low Ni concentration. The results for both $x = 0.125$ and $x = 0.25$ are presented in **Figure 9**. For $x = 0.25$, two distinct arrangements of Ni and Cu atoms in their respective sublattices are possible (refer to computational methods for cell construction details). In all considered scenarios, the Fermi level was found inside the bandgap. Consequently, in alignment with experimental findings, it can be inferred that a transition to n-type conductivity cannot be anticipated at these Ni concentrations, where Ni replaces Cu within the zinc blende crystal. Factors that could account for the discrepancy compared to ref. [10] include the incorporation of elemental Ni clusters, a higher overall Ni incorporation, or a phase transition to a different crystal structure. However, these factors were not accounted for in our calculations, due to their expected absence in the discussed experimental alloys. Another explanation of the n-type semiconducting $Ni_xCu_{1-x}I$ alloy, observed in literature, would be not completed iodization, where parts of the Ni-Cu thin films remain in their metallic state and therefore result in n-type Hall coefficient within a Hall effect measurement.

4. Conclusion

Within this work, $Ni_xCu_{1-x}I$ thin films were deposited by cosputtering in a reactive atmosphere and by PLD. An additional $NiI_2(H_2O)_6$ phase was observed in XRD for elevated Ni concentrations of $x \geq 0.31$. A reversible discoloration of the thin films from black to transparent was observed in ambient atmosphere, matching the deliquescent behavior of NiI_2, as described in ref. [15]. AFM images of the thin films show a transition from regular, triangular-shaped γ-CuI crystallites, to the appearance of a second phase toward a closed surface by this second phase with increasing Ni content, which can be attributed to the existence of the $NiI_2(H_2O)_6$ phase at the surface.

XPS analysis of element specific binding energies combined with Auger peak analysis revealed differences in the valence state of Ni regarding the surface and the bulk of the material. At the surface Ni^{2+} is recorded, suiting NiI_2 or its hydrated form being prevalent at the surface, as mentioned above. In the bulk of the

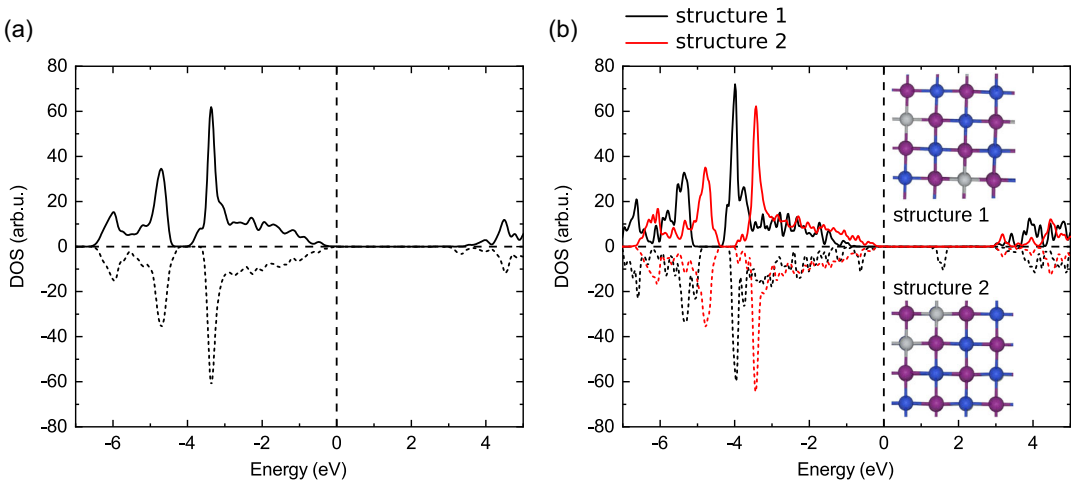

Figure 9. Calculated DOS with mHSE06 of $Ni_xCu_{1-x}I$ alloys for a) $x = 0.125$ and b) $x = 0.25$. In case of $x = 0.25$, in the considered setting of ordered alloys, the DOS of both distinct arrangements of Ni and Cu atoms in their sublattice are shown. The picture of the structure was produced with VESTA,[34] blue spheres represent Cu, gray Ni, and purple I.

thin films, elevated Ni concentrations of $x \geq 0.26$ lead to the detection of metallic Ni, which is confirmed by STEM measurements, where metallic Ni nanoclusters are detected. Along with these nanoclusters for elevated Ni concentrations, a multilayer structure in thin films of lower Ni concentrations of $x \approx 0.06$ and below is observed with Ni accumulations in between each single layer of about $10 - 20$ nm thickness.

For all thin films, a dilute magnetic behavior is observed. The saturation moment of the thin film with the highest Ni content exceeds the others by about an order of magnitude, which is attributed to the nanoscaled Ni clusters, observed in HRTEM for elevated Ni contents. However, a hysteresis loop cannot be observed, probably due to the spatial distribution, which isolates the Weiss domains of each Ni accumulation from each other, as superparamagnetism. Hall effect, resistivity, and Seebeck effect measurements revealed no transition to n-type, in contradiction to literature.[10] The persistent *p*-type character is also reinforced by DFT calculations, which found a Fermi level within the bandgap for up to $x = 0.25$. Therefore, the $Ni_xCu_{1-x}I$ alloy is no candidate for CuI-based homojunctions. However, the growth kinetics leading to self-organized layering of the structures, revealed in HRTEM, has to be further investigated as well as approaches to increase the solubility limit of Ni in CuI.

5. Experimental Section

$Ni_xCu_{1-x}I$ thin films were deposited by magnetron cosputtering from metallic Cu and Ni targets in a reactive $Ar + I_2$ atmosphere. The vacuum chamber was evacuated before each process to a base pressure of $p_{base} = 5.4 \times 10^{-5}$–$5.4 \times 10^{-4}$ mbar. The target to substrate distance was 15 cm, where the targets were located at the bottom of the chamber, opposite to the substrate holder, which was able to perform full turns to prevent compositional gradients. Solid iodine was stored in a secondary glass vacuum chamber, which was connected to the growth chamber via heated tubes. Infrared irradiation caused a sublimation of the solid iodine to its gaseous phase, which was then taken by an introduced Ar process gas flow from the secondary into the growth chamber.

The growth of the thin films was conducted at 2×10^{-2} mbar[24,25] for either 4 or 8 min and a constant electrical power at the Cu target of $P_{DC} = 90$ W. The optimal adjustments for homogeneous growth and desired crystallinity at an appropriate growth rate were determined to $p_{I_2} = 4 \times 10^{-3}$ mbar for the iodine partial pressure and RT as deposition temperature. The electrical power at the Ni target was varied from 2 to 70 W and between direct current (DC) and radio frequency (RF) mode, to result in $Ni_xCu_{1-x}I$ thin films with varying Ni contents *x*.

Furthermore, for direct comparison to literature,[10] a growth series was produced in the same vacuum chamber under inert Ar atmosphere, cosputtering from metallic Cu and Ni targets. The metallic–alloy thin films were exposed to postdeposition and ex situ iodization for 10 min in a Petri dish closed by a glas lid and filled with solid iodine. For sublimation of the solid iodine, the Petri dish was placed on a heat plate at $T = 90$ °C.

In addition to the sputtered films, $Ni_xCu_{1-x}I$ thin films were grown by PLD. The PLD source targets were prepared from CuI powder (Carl Roth 98 wt%) mixed with NiI_2 powder (Alfa Aesar 99.5 wt%). The homogenized powders were pressed into stainless steel forms at RT. The targets were not sintered but initially conditioned by the PLD excimer laser with at least 10 000 pulses. We used CuI targets with 0, 10, 20, 30, and 40 wt% NiI_2, which resulted in average Ni contents *x* of the $Ni_xCu_{1-x}I$ thin films of about 0.00, 0.04, 0.06, 0.14, and 0.22, respectively, as measured by EDX with 20 keV excitation energy. A large-area PLD setup with KrF laser was used as described for example in ref. [26]. Here, 6 000 or 8 000 laser pulses were applied in 3×10^{-3} mbar N_2 background gas to grow thin films simultaneously on rotating c-plane sapphire, Eagle XG glass, and NaCl (100) substrates at about 170 °C growth temperature. These PLD conditions were optimized in previous experiments, see refs. [7,13,27]. An additional series of PLD $Ni_xCu_{1-x}I$ films was deposited exactly like the aforementioned, but passivated by an additional Al_2O_3 capping layer, to prevent the undesired oxygen diffusion into the $Ni_xCu_{1-x}I$ thin films.[7,8] The capping layer was realized in situ by 2000 laser pulses on a polycrystalline Al_2O_3 target under the same conditions as the preceding $Ni_xCu_{1-x}I$ thin films.

2θ-ω scans were performed using a Philipps X'Pert X-Ray diffractometer with Cu Kα radiation. The global thin film composition was determined by EDX using a Bruker QUANTAX 200 with Flash 6 detector at an elevated excitation energy of 20 kV. Use of an excitation energy below 20 kV resulted in an overlap of the Ni and Cu signal, as shown in Figure S8–S10, Supporting Information. AFM scans were performed at a XE-150 Park Systems for surface analysis. Magnetization was measured via VSM at a physical probe measurement setup by Quantum Design, where an external magnetic field from $B = -9$ to 9 T was applied. All linear contributions, that is, from the diamagnetic substrate and possible paramagnetic contributions were removed within the data evaluation process. Subsequently the measured magnetization data (in emu) was normalized

to Bohr magnetons per unit cell (μ_B/u.c.) following the equation $M = \left(\frac{V_{film}}{a^3}\right)^{-1} \frac{M[emu]}{9.274\times10^{-21} emu/\mu_B}$. The volume was approximated by multiplying the homogeneous layer thickness by the area of each thin film, which was determined by a DektakXT profilometer and the use of a Keyence X-200 series laser scanning microscope. Hall effect and conductivity were measured in van-der-Pauw geometry, whereas separate, qualitative Seebeck effect measurements were conducted using a ME-22 T multimeter by Voltcraft and a soldering station.

The valence state of Ni at the surface as well as in the bulk of the thin films was determined by XPS, performed with a Thermofisher Nexsa G2 at Fraunhofer Institute IMWS, Halle (Saale), Germany. Therefore, survey spectra in the range of $E = 1350$ to -10 eV with an increment of 1 eV were recorded as well as detailed spectra of Cu 2p, Ni 2p, I 3 d, and Ni LM2 with an increment of 0.1 eV. The analysis at the bulk was conducted after sputtering in Ar^+ at 500 eV for 10 min at each thin film.

For studying the microstructure of the films cross-sectional area, a transmission electron microscope Thermo Fisher FEI Titan3 G2 80–300 (Hillsboro, Oregon, US) with 300 kV accelerating voltage was used, also at Fraunhofer IMWS, Halle (Saale), Germany. The scanning unit, together with HAADF detector, was applied to obtain STEM images. There, the contrast was partly dependent on the atomic number of the elements, that is, chemically sensitive. In combination with an energy dispersive X-ray spectroscopy (EDXS) detector Super-X, Thermo Fisher FEI (Hillsboro, Oregon, US) elemental mappings were generated. Spectra aquisition and further quantitative processing of the EDXS data was done utilizing the Esprit software Version 1.9 by Bruker, Billerica, US. In order to obtain electron transparent TEM samples, site-specific lift-out samples via FIB machining were prepared. To protect the film surface during the milling process, a thin carbon bar was deposited with the help of the electron beam before the actual platinum protection bar was deposited by cracking the precursor gas with the ion beam. After uncovering the lamella, it was transferred in situ with a needle to a Cu grid and thinned to electron transparency. Besides conventional TEM imaging, both, EDPs were recorded, and HRTEM was carried out, for visualization of atomic ordering.

Computational Section

All calculations were performed using DFT using the Vienna ab initio simulation package.[28,29] Pseudopotentials obtained through the projector-augmented wave method[30] were utilized. The valence electrons, explicitly treated, included the 4*s*, 3*p*, and 3*d* electrons of Cu and Ni, as well as the 5*s* and 5*p* electrons of I. We focused on describing ordered alloys, using $2\times2\times2$ primitive supercells (comprising 8 atoms of Ni and Cu each, along with 8 I atoms).With this computationally efficient approach, results in excellent agreement with experiments have already been obtained in the case of $Ag_xCu_{1-x}I$ alloys.[31]

A planewave basis set with a cutoff energy of 700 eV and a **k**-point grid of $4\times4\times4$ were used, satisfying a convergence criterion of 1 meV atom^{-1} for the total energy. Both, the crystal structure and the magnetic moments, were relaxed using the PBEsol functional[32] until all forces were less than 1 meV Å^{-1}. For the calculation of the DOS, we employed a mHSE06 with a fraction of Fock exchange energy $\alpha = 0.32$. The value of α was adjusted to make the mHSE06 functional replicate the bandgap of γ-CuI.[33] All computational analysis has been performed at Friedrich-Schiller-Universität Jena, Germany.

Supporting Information

Supporting Information is available from the Wiley Online Library or from the author.

Acknowledgements

The authors acknowledge funding by the Research Foundation: Deutsche Forschungsgemeinschaft (DFG, German Research Foundation) within the research unit FOR 2857, projects P01, P03, and P04. Computational resources were provided by the Leibniz Supercomputing Centre on Super MUC (project pn68le).

Open Access funding enabled and organized by Projekt DEAL.

Conflict of Interest

The authors declare no conflict of interest.

Data Availability Statement

The data that support the findings of this study are available from the corresponding author upon reasonable request.

Keywords

CuI-alloy, dilute magnetic semiconductor, high-resolution transmission electron microscopy, Ni doping, pulsed laser deposition, reactive co-sputtering, thin films

Received: October 27, 2023
Revised: December 18, 2023
Published online: January 21, 2024

[1] D. Chen, Y. Wang, Z. Lin, J. Huang, X. Chen, D. Pan, F. Huang, *Cryst. Growth Des.* **2010**, *10*, 2057.
[2] M. Kneiß, C. Yang, J. Barzola-Quiquia, G. Benndorf, H. von Wenckstern, P. Esquinazi, M. Lorenz, M. Grundmann, *Adv. Mater. Interfaces* **2018**, *5*, 6.
[3] C. Yang, M. Kneiß, M. Lorenz, M. Grundmann, *Proc. Natl. Acad. Sci. USA* **2016**, *113*, 12929.
[4] C. Yang, D. Souchay, M. Kneiß, M. Bogner, H. M. Wei, M. Lorenz, O. Oeckler, G. Benstetter, Y. Q. Fu, M. Grundmann, *Nat. Commun.* **2017**, *8*, 16076.
[5] M. Grundmann, F.-L. Schein, M. Lorenz, T. Böntgen, J. Lenzner, H. von Wenckstern, *Phys. Status Solidi A* **2013**, *210*, 1671.
[6] J. Wang, J. Li, S.-S. Li, *J. Appl. Phys.* **2011**, *110*, 054907.
[7] P. Storm, S. Gierth, S. Selle, M. S. Bar, H. von Wenckstern, M. Grundmann, M. Lorenz, *APL Mater.* **2021**, *9*, 051101.
[8] M. Lorenz, P. Storm, S. Gierth, S. Selle, H. von Wenckstern, M. Grundmann, *Chem. Ing. Tech.* **2023**, *95*, 11.
[9] M. Tsuji, S. Iimura, J. Kim, H. Hosono, *ACS Appl. Mater. Interfaces* **2022**, *14*, 33463.
[10] A. Annadi, N. Zhang, D. Boon Kiang Lim, H. Gong, *ACS Appl. Mater. Interfaces* **2020**, *12*, 6048.
[11] A. Annadi, H. Gong, *Appl. Mater. Today* **2020**, *20*, 100703.
[12] T. Jun, J. Kim, M. Sasase, H. Hosono, *Adv. Mater.* **2018**, *30*, 1706573.
[13] P. Storm, M. S. Bar, S. Selle, H. von Wenckstern, M. Grundmann, M. Lorenz, *Phys. Status Solidi RRL* **2021**, *15*, 2100214.
[14] T. Dietl, *Nat. Mater.* **2010**, *9*, 965.
[15] T. D. Siegler, L. C. Reimnitz, M. Suri, S. H. Cho, A. J. Bergerud, M. K. Abney, D. J. Milliron, B. A. Korgel, *Langmuir* **2019**, *35*, 2146.
[16] M. C. Biesinger, B. P. Payne, L. W. M. Lau, A. Gerson, R. C. St. Smart, *Surf. Interface Anal.* **2009**, *41*, 324.
[17] M. C. Biesinger, L. W. M. Lau, A. R. Gerson, R. S. C. Smart, *Phys. Chem. Chem. Phys.* **2012**, *14*, 2434.
[18] C. D. Wagner, L. H. Gale, R. H. Raymond, *Anal. Chem.* **1979**, *51*, 466.
[19] D. A. Keen, S. Hull, *J. Phys.: Condens. Matter* **1995**, *7*, 5793.

[20] S. Ackerbauer, N. Krendelsberger, F. Weitzer, K. Hiebl, J. C. Schuster, *Intermetallics* **2009**, *17*, 414.
[21] N. Teraguchi, A. Suzuki, Y. Nanishi, Y.-K. Zhou, M. Hashimoto, H. Asahi, *Solid State Commun.* **2002**, *122*, 651.
[22] R. Rajaram, A. Ney, G. Solomon, J. S. Harris, R. F. C. Farrow, S. S. P. Parkin, *Appl. Phys. Lett.* **2005**, *87*, 172511.
[23] J. K. Freericks, L. M. Falicov, *Phys. Rev. B* **1992**, *45*, 1896.
[24] C. Yang, E. Rose, W. Yu, T. Stralka, F. Geng, M. Lorenz, M. Grundmann, *ACS Appl. Electron. Mater.* **2020**, *2*, 3627.
[25] W. Yu, G. Benndorf, Y. Jiang, K. Jiang, C. Yang, M. Lorenz, M. Grundmann, *Phys. Status Solidi RRL* **2021**, *15*, 2000431.
[26] M. Lorenz, H. Hochmuth, H. von Wenckstern, M. Grundmann, *Rev. Sci. Instrum.* **2023**, *94*, 083905.
[27] P. Storm, M. S. Bar, G. Benndorf, S. Selle, C. Yang, H. von Wenckstern, M. Grundmann, M. Lorenz, *APL Mater.* **2020**, *8*, 091115.
[28] G. Kresse, J. Furthmüller, *Comput. Mater. Sci.* **1996**, *6*, 15.
[29] G. Kresse, D. Joubert, *Phys. Rev. B* **1999**, *59*, 1758.
[30] P. E. Blöchl, *Phys. Rev. B* **1994**, *50*, 17953.
[31] E. Krüger, M. Seifert, V. Gottschalch, H. Krautscheid, C. S. Schnohr, S. Botti, M. Grundmann, C. Sturm, *AIP Adv.* **2023**, *13*, 035117.
[32] J. P. Perdew, A. Ruzsinszky, G. I. Csonka, O. A. Vydrov, G. E. Scuseria, L. A. Constantin, X. Zhou, K. Burke, *Phys. Rev. Lett.* **2008**, *100*, 136406.
[33] M. Seifert, T. Rauch, M. A. L. Marques, S. Botti, ArXiv arXiv:2305.14941 [cond–mat.mtrl–sci].
[34] K. Momma, F. Izumi, *J. Appl. Cryst* **2011**, *44*, 1272.